

Sodium Metasilicate-Based Inorganic Composite for Heterogeneous Integration of Microsystems

James C. McRae¹, Melissa A. Smith¹, *Member, IEEE*, Bradley P. Duncan¹, Eric Holihan,
Vladimir Liberman, Caitlin Rock, Devon Beck, and Livia M. Racz¹

Abstract—Electronic microsystems are foundational to today’s computational, sensing, communication, and information processing capabilities, therefore impacting industries, such as microelectronics, chemical, healthcare, manufacturing, and aerospace. As demand grows for more capable microsystems to help address today’s rapidly growing needs, new packaging materials that are compatible with high-precision silicon microfabrication must be developed in order to enable the integration of individual and disparate components into systems with complex functionality. This article aims to demonstrate the potential for using a silicate-based inorganic composite to encapsulate and three-dimensionally integrate individual components into complex systems in a heterogeneous 3-D integration approach. Through the use of liquid alkali sodium silicate (water glass) and nanoparticle fillers, composites can be synthesized and cured at low temperatures into chemically, mechanically, and thermally (up to 400 °C) stable structures using high-throughput processing methods, such as spin and spray coating. This work demonstrates that this material can be processed into thick layers (tens to hundreds of micrometers), can fill high aspect ratio gaps (13:1), can withstand common microfabrication processes (wet process chemicals, photolithography, polishing, and thermal stability), and have its coefficient of thermal expansion tailored for compatibility with a variety of substrates. These demonstrations position this composite material for use in heterogeneous 3-D integration approaches that enable a wider range of complex microsystems.

Index Terms—Gap fill, heterogeneous integration, inorganic composite, molding material, silicate.

I. INTRODUCTION

THERE is a growing demand for smaller electronic systems with low mass and volumes that consume less power, without sacrificing functionality and complexity [1]–[3]. Traditional approaches for enabling complexity and functionality, i.e., microfabrication and packaging, are limited by fabrication tooling constraints (contamination and process temperature) or density of active system components that

can be integrated (MEMS, microfluidics, microprocessors, and power electronics). One emerging effort to address challenges in heterogeneous integration is the “chiplet” approach where reusable, smaller, cheaper, and modular microsystems with various functionalities could all be snapped into a universal bus to create a multifunctional system [3]. Alternatively, 3-D integration has existed as a more mature method for allowing greater volumetric packaging efficiency of varied and disparate components and shorter interconnects, therefore enabling complex functionality and improved efficiency with simpler designs for electronic systems [4]–[7]. Current 3-D integration techniques include through-silicon vias (TSV), die bonding, and molding [8]–[13]. Molding is of particular interest as it is commonly used in fan-out wafer-level packaging (FOWLP) and fan-out panel-level packaging (FOPLP) to integrate and encapsulate commercial off-the-shelf (COTS) components into high-density packages [2], [14], [15]. Ultimately, epoxy molding compounds (EMCs) have the potential to enable components to be heterogeneously 3-D-integrated into highly capable microsystems that benefit from 3-D integration without needing components to be specially designed for it. Common commercial EMCs have coefficients of thermal expansion (CTEs) of around 10 ppm/°C [14], with some EMCs in the literature reporting CTE of approximately 6 ppm/°C [16] and glass transition temperatures (T_g) ranging from 130 °C to 200 °C [16], [17]. However, these EMCs face considerable challenges due to CTE mismatch and low T_g that lead to warpage, thermal stress build-up, component shifting, and, ultimately, strict limitations on processing temperatures after the postmold cure (PMC) [2], [14]–[21].

Therefore, for a molding material to support this heterogeneous 3-D integration approach, it must meet the following criteria.

A. Low-Temperature and High-Throughput Processing

The material must be processed at low temperatures to remain within the thermal budget of COTS die (400 °C). In addition, this material must be compatible with high-throughput processing techniques, such as spray coating or spin coating in order to be cost-effective.

B. Thick Layer Processing

The material must be capable of being formed into a thick layer (tens to hundreds of micrometers) in order to completely encapsulate die and provide the next surface for

Manuscript received July 17, 2020; revised October 27, 2020; accepted December 1, 2020. Date of publication December 8, 2020; date of current version January 25, 2021. This work was supported by the Under Secretary of Defense for Research and Engineering under Air Force Contract No. FA8702-15-D-0001. Recommended for publication by Associate Editor K. Sakuma upon evaluation of reviewers’ comments. (*Corresponding author: James C. McRae.*)

James C. McRae was with the MIT Lincoln Laboratory, Lexington, MA 02420 USA. He is now with the Massachusetts Institute of Technology (MIT), Cambridge, MA 02139 USA (e-mail: jcmcrae@mit.edu).

Melissa A. Smith, Bradley P. Duncan, Eric Holihan, Vladimir Liberman, Caitlin Rock, Devon Beck, and Livia M. Racz are with the MIT Lincoln Laboratory, Lexington, MA 02420 USA (e-mail: melissa.smith@ll.mit.edu).

Color versions of one or more figures in this article are available at <https://doi.org/10.1109/TCPMT.2020.3043367>.

Digital Object Identifier 10.1109/TCPMT.2020.3043367

subsequent microfabrication in the three-dimensionally integrated microsystem.

C. Gap Fill

The material must completely fill gaps (<10- μm wide and >50- μm deep) between die components so that there are no voids or air pockets throughout the entire package, and structural integrity is maintained.

D. Microfabrication Compatibility and Thermal Stability

The material must be compatible with common microfabrication processes, such as wet cleans, etches, high-temperature microfabrication processes (up to 400 °C), and photolithographic patterning. Furthermore, the material must be planarizable for subsequent photolithographic processes.

E. Coefficient of Thermal Expansion Compatibility

The CTE of the material must be tunable to prevent stress build-up and potential cracking or delamination when used on common substrate materials (silicon, gallium arsenide, and so on). Generally, the CTE should be below 10 ppm/°C for consideration as a molding material [8].

Current alternatives to typical EMC do not meet all necessary criteria as they are too thin (<2 μm) to behave as a structural packaging material [22], [23] or are made from organic polymer materials that limit their usefulness in harsh environments [24]–[27].

This work aims to demonstrate the potential for an inorganic silicate composite, comprised of liquid alkali sodium silicate and nanoparticle fillers, to support this heterogeneous 3-D integration approach [28], [29]. Liquid alkali sodium silicate glass, commonly referred to as “water glass,” is a suitable precursor for a packaging composite because it can form a robust inorganic glass and, due to its low viscosity prior to curing, has the potential to fill high aspect ratio gaps between die and components to provide structural integrity to the heterogeneously integrated microsystem.

Previous work shows similar silicate composites being used as coatings, binders, and adhesives for ceramics, metals, quartz, and glass, indicating good adhesion properties with common IC chip materials [30]–[43]. In addition, for use as an electronic packaging composite, the liquid alkali sodium silicate must be processed into a neutral glass to induce curing and form a rigid structure that is chemically, mechanically, and thermally stable [44], [45]. Common methods for curing silicate materials, such as adding water or acid, are not viable for encapsulation because adding water will create excess volume change when curing and acids tend to liberate silica from the silicate matrix, compromising mechanical integrity [44]. In this work, silica nanoparticle fillers were added to induce curing [44], [46]. The addition of silica nanoparticles lowers the alkalinity due to the slight dissolution of silica and an overall reduction in sodium content. This results in dense silicate–silica matrix–filler composite with more bridging oxygen atoms around the tetrahedral silicon than liquid alkali sodium silicate [44]. Fig. 1 highlights this process.

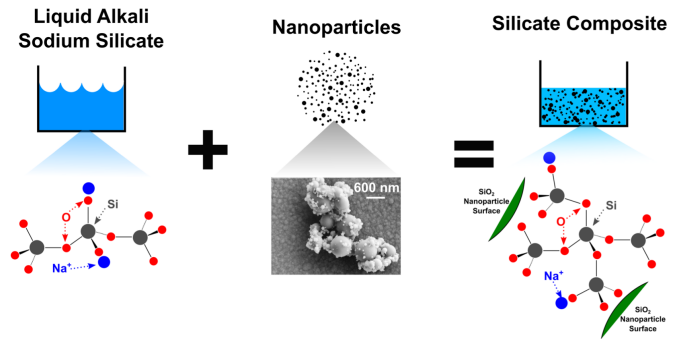


Fig. 1. Illustration of silicate composite formulation via the addition of a silica nanoparticle filler, not to scale. Slight dissolution of SiO₂ in alkali solution creates a branched, rigid silicate matrix with four bridging oxygen atoms, as opposed to two in alkali solution [44].

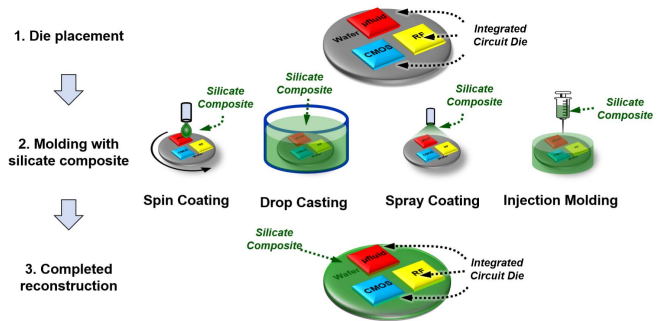


Fig. 2. Chart depicting processing options for silicate composite.

The addition of silica nanoparticles provides additional important advantages. First, they can be used to tailor the CTE to better match common substrates (silicon, gallium arsenide, and so on) [20], [47], [48]. Second, they can be used to tune the viscosity, making this material extremely versatile for many low-temperature processing techniques, such as drop casting, spin coating, spray coating, and injection molding, as shown in Fig. 2. This work mainly focuses on silicate composites processed via spin coating and spray coating.

Finally, in order to cure the silicate composite, the water must be removed from the film. Since water removal is the sole curing mechanism required after the addition of silica nanoparticles, this process can be done at very low temperatures (approximately 100 °C). Complete removal of water is vital to the mechanical and chemical integrity of the composite because hydrated silicate materials are susceptible to dissolution [44]. The optimal curing conditions (temperature, heating rate, time, and gaseous environment) will greatly depend upon the composite composition, processing method, and application.

The following will be organized around the five criteria described in this introduction. We will describe how we tested these criteria in Section II, followed by a demonstration and discussion of the composite’s ability to meet these criteria in Section III.

II. EXPERIMENTAL

A. Low-Temperature and High-Throughput Processing

To demonstrate high-throughput and low-temperature processing, silicate solutions were formulated for spray coating

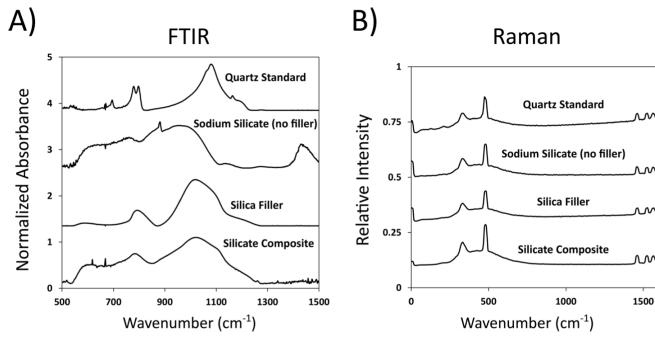


Fig. 3. (a) FTIR spectra comparing quartz standard to the individual composite components (sodium silicate and silica filler) and the silicate composite. (b) Raman spectra comparing quartz standard to the individual composite components (sodium silicate and silica filler) and the silicate composite.

and spin coating. Silicate composite solutions were made by mixing different variations of silica particles (800-nm silica from the US Research Nanomaterials, Inc.; Aerosil 200 from Evonik) with reagent grade sodium silicate (Sigma-Aldrich Reagent Grade). Mixing was done using a Flacktek Inc. Speedmixer model DAC 600.2VAC-LR at 4000 rpm for 5 min. Spin coating was done by spinning 1 mL of 50% by weight of 800-nm silica in reagent grade sodium silicate onto a 50 mm × 50 mm silicon substrate with 500–1000 nm of PECVD oxide at 5000 rpm for 1 min. After spinning, the sample was cured on a hot plate brought from room temperature to 200 °C at approximately 20 °C/min. The sample was held at 200 °C for approximately 5 min. This curing process was chosen over a lower temperature process in order to more rapidly process samples. Spray coating was done using a Sono-Tek Exactacoat 25 kHz Focused Tip with AccuMist to deposit three different composite compositions: 1) reagent grade sodium silicate without nanoparticle loading; 2) 2.5% by weight of Aerosil 200 in sodium silicate; and 3) 30% by weight of 800-nm silica in sodium silicate. Samples were left at room temperature for approximately one week before measurements and characterization. The structure of the silicate composite was analyzed using absorbance mode FTIR-ATR (Bruker Vertex 70 with Platinum ATR) and Raman spectroscopy (Renishaw InVia Confocal Raman Microscope) with a 532-nm laser at 1% intensity over 100 scans on quartz standard (Sigma Aldrich), reagent grade sodium silicate, silica filler, and the silicate composite. This is shown in Fig. 3. For FTIR, broad peaks at 800 cm⁻¹ indicate Si–O bonding (present in silica filler and composite), and peaks at 1100 cm⁻¹ indicate Si–O–Si bonding (present in quartz standard, silica filler, and composite). The lack of a peak at 1100 cm⁻¹ in the sodium silicate indicates that there is minimal branched Si–O–Si bonding. Adding silica filler to formulate the composite results in a Si–O–Si peak, indicating a more branched network in the composite compared with the reagent grade sodium silicate. The broad peaks around 1000 cm⁻¹ is characteristic of amorphous glass materials. For Raman, the spectra are nearly identical between all samples. Raman peaks at 333 and 465 cm⁻¹ represent symmetric Si–O–Si stretching, again indicating a branched silicate network.

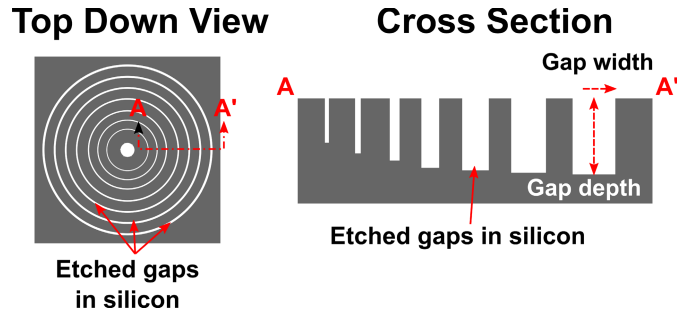


Fig. 4. Depiction of gap-fill substrates where concentric rings are etched into silicon to create various aspect ratio gaps.

B. Thick Layer Processing

Thick layer samples were prepared by cleaving standard [001] silicon wafers with 500–1000 nm of plasma-enhanced chemical vapor deposition (PECVD) silicon dioxide or thermally grown silicon dioxide and cleaned with O₂ plasma. The silicon oxide films protected the underlying silicon from being etched by the alkali silicate solution.

Spin- and spray-coating processes were used to deposit single and multilayer films. For spin coat layering, the previously described spin-coat process was performed three consecutive times on the same sample, with an acetone and isopropyl alcohol (IPA) rinse followed by an O₂ plasma clean (300 W and 10 min) prior to each deposition. Spray coat layers were deposited and cured using the previously described spray coat process with multiple deposition passes over the substrate. Spray coating was also used for thick single layer deposition using the previously described method with an increased volume flow rate.

C. Gap Fill

Gap-fill test substrates were fabricated to test the silicate composite's ability to fill gaps and voids. The substrate fabrication was done using a subtractive Bosch etch to etch a concentric ring pattern, as shown in [11], into silicon to generate test gaps. This is represented in Fig. 4.

The line thickness and etch depths of these concentric rings translate to the gap width and gap depth, respectively. Line widths range from approximately 5–50 μm, and etch depths range from approximately 50–100 μm. A thermal oxide layer was then grown to protect the underlying silicon from being etched by the alkali silicate solution.

Spray coating was selected to demonstrate the silicate gap-filling capability. The samples were cleaned and exposed to O₂ plasma before deposition of the silicate composite to clean the surface and make it hydrophilic. After deposition, samples were left at room temperature for approximately one week before substrates were cleaved for cross section analysis. Morphology and gap fill were characterized using scanning electron microscopy (Zeiss Gemini SEM). Reagent grade sodium silicate and 30% by weight of 800-nm silica composites were analyzed to determine the gap-filling ability of the composite with and without nanoparticle filler.

D. Microfabrication Compatibility

Spin coat samples as previously described were used for compatibility testing with common microfabrication procedures, as described in the following.

1) *Wet Etch and Solvent Clean Processing*: Wet etch and solvent clean procedures are outlined in this section.

Aqua Regia: Nitric acid (75 mL, 70% from Honeywell) was added to hydrochloric acid (225 mL, 36.5%–38% from J. T. Baker) and mixed well. The silicate sample was then added to the bath for 20 min. After removal, the sample was rinsed in deionized water and dried in N₂.

Nitric Acid: It (65 mL, 70% from Honeywell) was added to deionized water (300 mL) and stirred well. The silicate sample was then placed in the bath for 20 min. After removal, the sample was rinsed in deionized water and dried in N₂.

Piranha: Hydrogen peroxide (30 mL, 30% from Honeywell) was added to sulfuric acid (80 mL, 96% J. T. Baker) and was stirred until completely mixed. The solution was then heated to approximately 80 °C, at which time the silicate sample was added for 10 min. The solution was maintained at approximately 80 °C ± 5 °C. After piranha cleaning, the sample was rinsed in deionized water and dried in N₂.

SC2: Hydrochloric acid (25 mL, 36.5%–38% from J. T. Baker) was added to deionized water (150 mL) and heated to approximately 70 °C. Hydrogen peroxide (25 mL, 30% from Honeywell) was then added to the solution. After waiting for 2 min, the sample was placed in the bath for 10 min while maintaining a temperature at 70 °C ± 5 °C. After removal, the sample was rinsed in deionized water and dried in N₂.

Acetone: A sample was placed in an acetone bath for 20 min at room temperature and subsequently dried with N₂.

IPA: A sample was placed in an IPA bath for 20 min at room temperature and subsequently dried with N₂.

Deionized Water: A sample was placed in a deionized water bath for 20 min at room temperature and subsequently dried with N₂.

SC1: Ammonium hydroxide (22 mL, 29% from J. T. Baker) was added to deionized water (110 mL) and heated to approximately 70 °C. Hydrogen peroxide (22 mL, 30% from Honeywell) was then added to the solution. After waiting for 2 min, the sample was placed into the bath for 10 min while maintaining the temperature at 70 °C ± 5 °C. After removal, the sample was rinsed in deionized water and dried in N₂.

Hydrofluoric Acid: It (49% from J. T. Baker) was diluted in deionized water at a volume ratio of 10:1 H₂O:HF. The silicate sample with patterned resist was then placed into the HF for 5 min. After the etch bath, the sample was rinsed in deionized water, followed by acetone resist strip, IPA rinse, and N₂ dry.

TMAH: Tetramethylammonium hydroxide (50 mL, 25% from Sigma-Aldrich) was added to deionized water (108 mL), mixed well, and heated to approximately 80 °C. The silicate sample with patterned resist was added to the bath for 30 min while maintaining a bath temperature of 80 °C ± 5 °C. After the bath, the sample was rinsed with deionized water and dried in N₂.

O₂ Plasma: The samples were placed in GaSonic O₂ plasma asher at 300-W power for 10 min. The max temperature reached is approximately 100 °C.

Thermal Stability: Cured silicate samples were subject to 400 °C on a hot plate for 30 min.

2) *Photolithography and Patterning*: A spin-coated sample was used for patterning. AZ 1529 resist was spun at 4000 rpm to a thickness of 2.9 μm. This resist was then baked at 100 °C for 3 min, exposed using an OAI Model 808 Mask Aligner for 20 s using an arbitrary mask with feature sizes on the order of millimeters in width, developed for 90 s in AZ 300 MIF developer and postbaked at 110 °C for 3 min. This silicate sample with patterned resist was then placed in a 10:1 DI H₂O:HF bath for 5 min at room temperature for etching. Finally, the resist was stripped with acetone followed by IPA and N₂ to dry.

3) *Polishing*: A three-layer spin coat sample (~26 μm) was polished via mechanical polishing methods in a three-step process using Logitech Precision Lapping & Polishing systems. The substrate was mounted parallel on a polished glass carrier in a crystal bond wax. The initial stage polish was done to planarize the surface area by using a Logitech PM5 precision lapping and polishing system with a cast iron wheel and an abrasive alumina microgrit slurry for 10 min. The second stage polish was done by using a Logitech LP50 precision lapping and polishing system with a slotted felt pad and a diamond-alumina microgrit slurry for 2 h. The final stage polish was done using a Logitech LP50 precision lapping and polishing system with the same slotted pad as stage two, using a colloidal silica-based polishing slurry for 1 h. Composite surface profiles were obtained using both a Keyence 3-D Laser Microscope and a Zygo 3-D Optical Profiler.

E. Coefficient of Thermal Expansion Tuning

To demonstrate CTE engineering via nanoparticle loading, a composite silicate material was designed and formulated to bring its CTE closer to that of silicon (2.6 ppm/°C). The 50% by weight of 800-nm silica nanoparticles in sodium silicate was deposited on silicon and gallium arsenide of 50-mm wafers via spin coating. Prior to deposition on gallium arsenide, a 300-nm PECVD oxide was deposited to promote adhesion to the substrate. The solutions were deposited on the unpolished backside of the wafer in order to leave the polished surface available for reflective laser measurements. The samples were then cured in a dry room temperature environment for 2 h, followed by 93 °C cure for 4 h and a 275 °C cure for 30 min. Each sample was subjected to stress–temperature measurement using a Toho FLX 2320-S Thin Film Stress Measurement tool. This test ramps the samples up to 400 °C and back to room temperature while intermittently measuring the substrate bow via laser reflections to calculate stress. The heating profile was: 5 °C/min until 100 °C, 8 °C/min until 200 °C, and 16 °C/min until 400 °C. The cooling profile was the reverse order. The CTE was then estimated using this experimental data via methods described in Toho FLX 2320-S user manual chapters 7.2 and 9 and [49], [50].

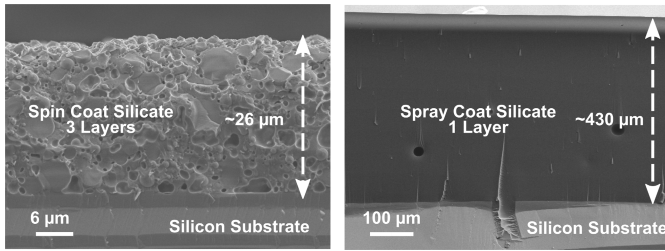


Fig. 5. SEM micrographs depicting a thick three-layer film ($\sim 26 \mu\text{m}$; 50% by weight of nanoparticle filler) via spin coating and a thick single layer ($\sim 430 \mu\text{m}$; no filler loading) via spray coating.

III. RESULTS

A. Thick Layer Processing

Thick silicate composite layers were successfully created through layer-by-layer stacking and single layer processing. Fig. 5 demonstrates the thick film processing results via spin coating and spray coating. The spin coating produced individual films of approximately $8\text{--}10 \mu\text{m}$ that were stacked into one $26\text{-}\mu\text{m}$ -thick film with no discernable seams or interfaces between layers. This indicates that the deposited liquid silicate layer slightly dissolves the underlying silicate layer before curing. Spray-coated reagent grade sodium silicate without nanoparticle filler produced a single layer that is hundreds of microns thick.

Small voids formed within the spin-coated composite while curing, likely due to water evaporation during rapid heating from room temperature to 200°C while curing. It is suspected that these voids can be prevented using a lower temperature ($<100^\circ\text{C}$), dry N_2 cure over a longer time period. The hot plate cure was preferred in this work due to its ability to process films quickly. The void present in the spray-coated sample is, based on SEM inspection, highly uncommon and not representative of the bulk spray-coated silicate films. It is suspected that any gas trapped within the voids during processing can be safely evacuated, as these films were placed in a vacuum (4×10^{-7} Torr) for multiple hours and showed no structural or mechanical changes.

B. Gap Fill

Ultrasonic spray coating was successful at filling gaps with various composite compositions, as depicted in Fig. 6. Using ultrasonic spray coating, the reagent grade sodium silicate filled gaps at aspect ratios ranging from 2:1 to 13:1 without any voids, with dimensions of the highest aspect ratio gap being approximately $4\text{-}\mu\text{m}$ wide \times $55\text{-}\mu\text{m}$ deep. In addition, silicate composites with high particle loading (30% by weight of 800-nm silica nanoparticles) filled gaps at aspect ratios of approximately 7:1.

The silicate composite's gap-filling ability is attributed to the combination of the ultrasonic spray coating and the material viscosity upon deposition. The ultrasonic spray-coating process deposits droplets that are small enough to fill these narrow and high aspect ratio gaps, and the low viscosity allows the material to easily flow into the gaps before curing.

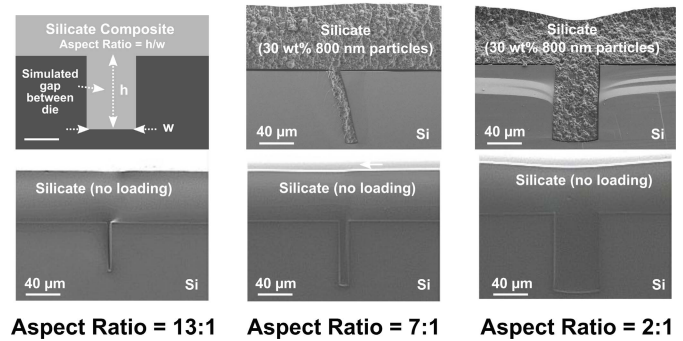


Fig. 6. SEM micrographs depicting silicate gap fill at various aspect ratios with and without silica nanoparticle filler.

C. Microfabrication and Thermal Compatibility

1) *Wet Process and Temperature Compatibility:* Visual inspections were done to evaluate the compatibility of the silicate material with various wet clean processes and high-temperature exposure. Fig. 7 summarizes the results of the wet process compatibility testing. Low-pH processes, specifically nitric acid and piranha solution, compromised the film's mechanical integrity due to liberation of silica from the silicate matrix, as discussed in the literature [44]. The high-pH processes also compromised mechanical integrity, likely due to the solubility of silica and silicates in highly alkali solutions. The etch rate of this silicate composite in hydrofluoric acid was not precisely measured. However, it was estimated to etch at a rate of $2\text{--}5 \mu\text{m}/\text{min}$. In comparison, other standard microfabrication oxides, such as thermal and low-pressure chemical vapor deposition (LPCVD), etch at rates of tens and hundreds of nanometer/minute, respectively [51]. All other wet processes appear to have minimal or no effect on the silicate composite, based on visual inspection. In general, it is anticipated that this material will etch via the same processes as other common microfabrication oxides (thermal, LPCVD, and PECVD) but at a much faster rate due to the amorphous structure and composite network.

2) *Photolithography and Patterning:* The silicate material withstood photolithographic patterning and subsequent wet etching, as shown in Fig. 8.

There was a noticeable undercut from the etch that is typical of isotropic wet etch processes. The morphology of the composite after the etch is highlighted in Fig. 9. It is suspected that switching to a reactive ion etch (RIE) would minimize or eliminate the undercut and disparity in etch rate differences between the silicate binder and silica nanoparticles. It is speculated that the silicate binder etches extremely fast, while the wet bath washes away the now-loose silica particles. The SEM images in Fig. 9 indicate that the silicate matrix etched significantly faster than the silica particles. The region labeled as trace silica particles appears to contain interparticle voids that indicate where the silicate matrix previously was located compared with the bulk region where no voids are present.

3) *Polishing:* Mechanical polishing techniques were demonstrated to be effective in planarizing the as-deposited silicate composite, as shown in Fig. 10. The as-deposited

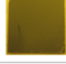

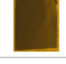
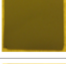




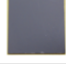











Process	Pre	Post	Estimated pH	Compatibility
Aqua Regia			<1	No effect
Nitric Acid			<1	Minimal change; splotchy white spots
Piranha			<1	Minimal change; turns slightly white
10:1 DI:HF			1.4	Fast etch (2-5 $\mu\text{m}/\text{min}$)
SC2			1.6	No effect
Acetone			~ 7	No effect
IPA			~ 7	No effect
DI Water			~ 7	No effect
SC1			~ 11	No effect
TMAH			>13	Dissolves completely
SC1 + SC2			N/A	No effect
O ₂ Plasma			N/A	No effect
400 °C			N/A	Turns whiter; No flaking or blistering

Fig. 7. Wet process and temperature compatibility.

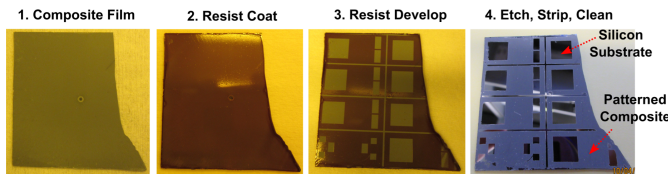


Fig. 8. Silicate composite at consecutive stages throughout a typical photoresist process.

silicate composite has a matte surface finish, whereas the polished silicate composite has a reflective surface finish. Surface profiles indicate that the estimated rms surface roughness was reduced from approximately 2.4 μm to approximately 50 nm after mechanical polishing. The rms surface roughness values of the polished sample excluded obvious defect areas shown by the darker regions in the profile.

D. Coefficient of Thermal Expansion

Silica nanoparticle fillers were effective at modifying the CTE of the composite to be compatible with silicon.

Fig. 11 depicts stress–temperature curves of the silicate composite on silicon and gallium arsenide substrates. The average stress–temperature derivatives, k_{Si} and k_{GaAs} , from

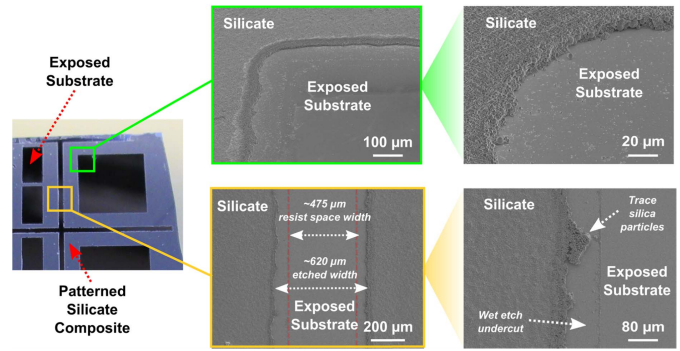


Fig. 9. SEM micrographs depicting the morphology of the silicate composite after the wet etch, highlighting the wet etch undercut and the tendency for the silicate matrix to etch faster than the silica nanoparticle filler.

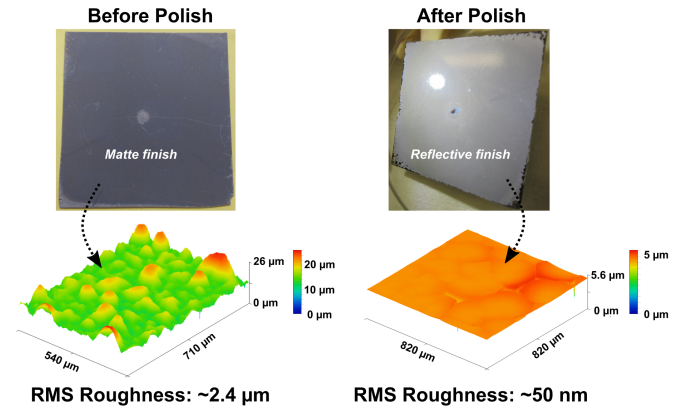


Fig. 10. Top: photographs comparing the silicate composite before and after mechanical polishing, with unpolished and polished samples having matte and reflective finishes, respectively. Bottom: surface profiles of silicate composite before and after polishing.

20 °C to 200 °C of the silicate composite were determined to be 0.0727 MPa/°C on silicon and -0.0282 MPa/°C on gallium arsenide. These values were used to estimate the CTE of the composite to be approximately 4.9 ppm/°C using methods from [50], as shown in the following equation:

$$k_{\text{Si}} = 0.0727 \text{ MPa}/^\circ\text{C} \quad (1)$$

$$k_{\text{GaAs}} = -0.0282 \text{ MPa}/^\circ\text{C} \quad (2)$$

$$\alpha_{\text{Si}} = 2.6 \text{ ppm}/^\circ\text{C} \quad (3)$$

$$\alpha_{\text{GaAs}} = 5.73 \text{ ppm}/^\circ\text{C} \quad (4)$$

$$\alpha_f = \frac{k_{\text{Si}} * \alpha_{\text{GaAs}} - k_{\text{GaAs}} * \alpha_{\text{Si}}}{k_{\text{Si}} - k_{\text{GaAs}}} \quad (5)$$

$$\alpha_f = 4.9 \text{ ppm}/^\circ\text{C}. \quad (6)$$

In addition, a rule of mixtures model was used to estimate the CTE of the composite to be approximately 3.9 ppm/°C. This was done using the calculations and associated assumptions shown in the following, where the individual CTE of the 800-nm silica nanoparticles (α_{silica}) and the reagent grade sodium silicate (α_{silicate}) were determined to be 0.64 and 12.72 ppm/°C, respectively, using linear approximation on results reported in Shermer's work [52]. This is shown in the following.

- 1) The solution is comprised of 10 g of silica nanoparticles and 10 g of reagent grade sodium silicate.

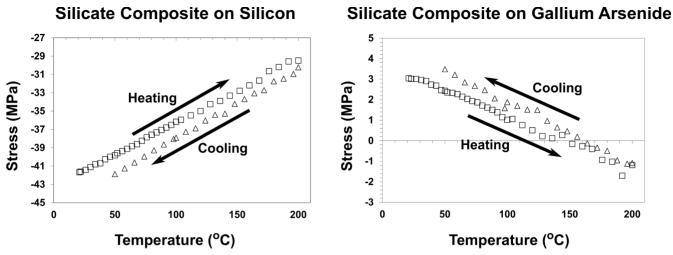


Fig. 11. Stress–temperature curves from 20 °C to 200 °C of 50% by weight of silica in sodium silicate on silicon (left) and gallium arsenide (right).

- 2) Reagent grade sodium silicate is 10.6% by weight of Na_2O , 26.5% by weight of SiO_2 , and 62.9% by weight of H_2O .
- 3) The ratio of silica to silicate in composite is maintained before and after spin coating.
- 4) The density of silica nanoparticles and SiO_2 in solution is 2.20 g/mL, and Na_2O in solution is 2.27 g/mL.
- 5) All water initially in reagent grade sodium silicate is removed during cure

$$\alpha_f = \frac{\alpha_{\text{silica}} * V_{\text{silica}} + \alpha_{\text{silicate}} * V_{\text{silicate}}}{V_{\text{composite}}} \quad (7)$$

$$\alpha_f = \frac{(0.64 \text{ ppm/C} * 4.55 \text{ mL}) + (12.72 \text{ ppm/C} * 1.67 \text{ mL})}{6.22 \text{ mL}} \quad (8)$$

$$\alpha_f = 3.9 \text{ ppm/}^\circ\text{C}. \quad (9)$$

The stress–temperature measurement data from 20 °C to 200 °C was extracted from an experimental data set that went up to 400 °C. This was done because, when curing, the silicate films reached a maximum temperature of approximately 275 °C. Therefore, stress values beyond 275 °C may have additional chemical or material dynamics occurring that may render the measured values inaccurate. This may help explain any variations between the heating and cooling curves.

The equations used to experimentally determine the CTE assume complete substrate coverage, perfect adhesion, and binary systems (one film on one substrate without any additional films). However, for samples used in this work, there is slight film flaking toward the middle of the sample due to the fact that, when spin-coated, the center of the substrate is not experiencing the same rotational dynamics as the outside of the wafer, resulting in slightly different drying characteristics of the silicate composite. After spin coating and before curing, the middle portion of the silicate film contains more water than the rest of the film, resulting in minor bubbling and flaking while curing. In addition, the silicate composite does not adhere well to the gallium arsenide substrate as it does on the silicon substrate. Therefore, a 300-nm PECVD oxide was deposited on the gallium arsenide prior to the composite to promote adhesion. The effects of these two deviations are assumed to be minimal because the flaked area is a very small percentage of the total substrate area and the PECVD oxide thickness (300 nm) is minimal compared with the thickness of the substrate ($\sim 300 \mu\text{m}$) and composite ($\sim 10 \mu\text{m}$) and, therefore, are not accounted for in CTE estimations. Given these deviations, it is concluded that the experimentally determined CTE of 4.9 ppm/°C and the estimated CTE of 3.9 ppm/°C

based on the rule of mixtures are generally in agreement and indicate that the CTE is low enough to be viable for heterogeneous integration in silicon-based microsystems.

IV. CONCLUSION

This inorganic silicate composite has been demonstrated as a promising molding material for heterogeneous 3-D integration that is mechanically, chemically, and thermally stable and, therefore, compatible with common microfabrication techniques (chemicals, photolithographic patterning, and polishing). Furthermore, this silicate composite has been shown to withstand temperatures of up to 400 °C and is expected to withstand even higher temperatures, indicating that it will not introduce thermal processing constraints. In addition, this silicate composite has shown to withstand vacuum as low as 3.6×10^{-7} Torr for multiple hours, indicating the suitability for use in vacuum. This silicate composite has shown to be suitable for spray coating and spin coating and is, therefore, assumed to be compatible with other low-temperature and high-throughput processing techniques, such as drop casting and injection molding. The silicate composite has been processed into thick films ranging from tens to hundreds of micrometers, which would allow for complete IC encapsulation for heterogeneous integration. It has demonstrated the ability to achieve conformal and high aspect ratio (13:1) gap fill with and without particle loading, another important feature necessary for the encapsulation of high-density components. Finally, the thermal expansion coefficient of this silicate composite has been estimated to be 4.9 ppm/°C, much lower than other EMC in the literature and within the compatible range for silicon substrates [8], [16], [20], [21], [48], [53]–[55].

Understanding the characteristics and capabilities of this silicate composite is vital to informing its integration into the fabrication of complex microsystems via a heterogeneous 3-D integration approach. Future work will explore optimizing curing procedures for a given composition, processing method, and application in order to reduce warpage and thermal stress, as well as negative-CTE particle loading for more flexibility with CTE matching, the impact that the anticipated high stiffness (Young’s Modulus) has on warpage, methods to prevent sodium ion contamination of encapsulated microsystems by exchanging Na^+ ions with NH_4^+ ions [56] or using nitride barrier layers, functional particle loading for uses outside of structural packaging material, and integration into other processing techniques.

ACKNOWLEDGMENT

DISTRIBUTION STATEMENT A: Approved for public release. Distribution is unlimited. This material is based upon work supported by the Under Secretary of Defense for Research and Engineering under Air Force Contract No. FA8702-15-D-0001. Any opinions, findings, conclusions, or recommendations expressed in this material are those of the author(s) and do not necessarily reflect the views of the Under Secretary of Defense for Research and Engineering. The authors would like to thank Sono-Tek Corporation for developing spray coat procedures for the silicate composite.

REFERENCES

- [1] S. J. Koester *et al.*, "Wafer-level 3D integration technology," *IBM J. Res. Dev.*, vol. 52, no. 6, pp. 583–597, 2008.
- [2] J. H. Lau *et al.*, "Warpage and thermal characterization of fan-out wafer-level packaging," *IEEE Trans. Compon., Packag., Manuf. Technol.*, vol. 7, no. 10, pp. 1729–1738, Oct. 2017.
- [3] G. Mounce, J. Lyke, S. Horan, W. Powell, R. Doyle, and R. Some, "Chiplet based approach for heterogeneous processing and packaging architectures," in *Proc. IEEE Aerosp. Conf.*, Mar. 2016, pp. 1–12.
- [4] P. Ramm, J. Lu, and M. Taklo, *Handbook Wafer Bonding*. Hoboken, NJ, USA: Wiley, 2012.
- [5] E. Beyne, "3D system integration technologies," in *Proc. Int. Symp. VLSI Technol., Syst., Appl.*, Apr. 2006, pp. 1–9.
- [6] E. Beyne, "The 3-D interconnect technology landscape," *IEEE Des. Test. IEEE Des. Test. Comput.*, vol. 33, no. 3, pp. 8–20, Jun. 2016.
- [7] M. Rimskog, "Through wafer via technology for MEMS and 3D integration," in *Proc. 32nd IEEE/CPMT Int. Electron. Manuf. Technol. Symp.*, Oct. 2007, pp. 286–289.
- [8] K. Kan, M. Sugahara, and M. Cichon, *The Role of Liquid Molding Compounds in the Success of Fan-Out Wafer-Level Packaging Technology*. Hoboken, NJ, USA: Wiley, 2019, ch. 13, pp. 261–270.
- [9] M. Lapisia, G. Stemme, and F. Niklaus, "Wafer-level heterogeneous integration for MOEMS, MEMS, and NEMS," *IEEE J. Sel. Topics Quantum Electron.*, vol. 17, no. 3, pp. 629–644, May 2011.
- [10] *International Technology Roadmap for Semiconductors*, ITRS Group Ltd., London, U.K., 2015.
- [11] M. A. Smith *et al.*, "A low-temperature nickel silicide process for wafer bonding and high-density interconnects," *IEEE Trans. Compon., Packag., Manuf. Technol.*, vol. 10, no. 5, pp. 908–916, May 2020.
- [12] M. Brunnbauer *et al.*, "An embedded device technology based on a molded reconfigured wafer," in *Proc. 56th Electron. Compon. Technol. Conf.*, May 2006, p. 5.
- [13] T. Wang *et al.*, "Wafer reconstruction: An alternative 3D integration process flow," in *Proc. IEEE 15th Electron. Packag. Technol. Conf. (EPTC)*, Dec. 2013, pp. 415–419.
- [14] J. H. Lau, "Recent advances and trends in fan-out wafer/panel-level packaging," *J. Electron. Packag.*, vol. 141, no. 4, Dec. 2019, Art. no. 040801.
- [15] J. H. Lau *et al.*, "Panel-level fan-out RDL-first packaging for heterogeneous integration," *IEEE Trans. Compon., Packag., Manuf. Technol.*, vol. 10, no. 7, pp. 1125–1137, Jul. 2020.
- [16] K. Kwon *et al.*, "Compression molding encapsulants for wafer-level embedded active devices: Wafer warpage control by epoxy molding compounds," in *Proc. IEEE 67th Electron. Compon. Technol. Conf. (ECTC)*, May 2017, pp. 319–323.
- [17] H. Jeong, K.-H. Jung, C.-J. Lee, K. D. Min, W.-R. Myung, and S.-B. Jung, "Effect of epoxy mold compound and package dimensions on the thermomechanical properties of a fan-out package," *J. Mater. Sci., Mater. Electron.*, vol. 31, no. 9, pp. 6835–6842, May 2020.
- [18] E. K. Th *et al.*, "Encapsulation challenges for wafer level packaging," in *Proc. 11th Electron. Packag. Technol. Conf.*, Dec. 2009, pp. 1–6.
- [19] F. X. Che, D. Ho, M. Z. Ding, and X. Zhang, "Modeling and design solutions to overcome warpage challenge for fan-out wafer level packaging (FO-WLP) technology," in *Proc. IEEE 17th Electron. Packag. Technol. Conf. (EPTC)*, Dec. 2015, pp. 1–8.
- [20] J. Park *et al.*, "Fabrication and characterization of epoxy molding films (EMFs) for wafer-level and panel-level fan out packages," in *Proc. IEEE 68th Electron. Compon. Technol. Conf. (ECTC)*, May 2018, pp. 712–717.
- [21] A. Kumar *et al.*, "Wafer level embedding technology for 3D wafer level embedded package," in *Proc. 59th Electron. Compon. Technol. Conf.*, May 2009, pp. 1289–1296.
- [22] *Spin-on Glass NDG-7000: Data Sheet*, Desert Silicon, Tempe, AZ, USA, 2018.
- [23] *Information About FOx-1x FOx-2x Flowable Oxides: Product Information*, Dow Corning, Midland, MI, USA, 1997.
- [24] A. D. Campo and C. Greiner, "SU-8: A photoresist for high-aspect-ratio and 3D submicron lithography," *J. Micromech. Microeng.*, vol. 17, no. 6, pp. R81–R95, May 2007.
- [25] *NANOTM SU-8 Negative Tone Photoresist Formulations 2-25: Data Sheet*, MicroChem, Okhla, New Delhi, 2019.
- [26] N. Ahner, S. E. Schulz, F. Blaschta, and M. Rennau, "Thermal stability and gap-fill properties of spin-on MSQ low-k dielectrics," *Microelectron. Eng.*, vol. 84, no. 11, pp. 2606–2609, Nov. 2007.
- [27] M. J. Loboda, "Properties of a-SiO[sub x]:H thin films deposited from hydrogen silsesquioxane resins," *J. Electrochem. Soc.*, vol. 145, no. 8, p. 2861, 1998.
- [28] M.-R. Yuan, J.-T. Lu, and G. Kong, "Effect of SiO₂:Na₂O molar ratio of sodium silicate on the corrosion resistance of silicate conversion coatings," *Surf. Coatings Technol.*, vol. 204, no. 8, pp. 1229–1235, Jan. 2010.
- [29] T. Luukkonen *et al.*, "Influence of sodium silicate powder silica modulus for mechanical and chemical properties of dry-mix alkali-activated slag mortar," *Construct. Building Mater.*, vol. 233, Feb. 2020, Art. no. 117354.
- [30] *PELCO High Performance Ceramic Adhesive, 1 Pint or 50 g Product No. 16026, 16026-10: Technical Notes*, PELCO, Fresno, CA, USA, 2012.
- [31] A. A. Shores, "Moisture getting composition for hermetic microelectronic devices," U.S. Patent 5591379A, Jan. 7, 1997.
- [32] Y. Xu, X. Luo, and D. D. L. Chung, "Sodium silicate based thermal interface material for high thermal contact conductance," *J. Electron. Packag.*, vol. 122, no. 2, pp. 128–131, Jun. 2000.
- [33] A. Brough and A. Atkinson, "Sodium silicate-based, alkali-activated slag mortars: Part I. Strength, hydration and microstructure," *Cement Concrete Research*, vol. 32, no. 6, pp. 865–879, 2002.
- [34] D. Hillman, R. Wilcoxon, N. Lower, and D. Grossman, "Alkali silicate glass coatings for mitigating the risks of tin whiskers," *J. Electron. Mater.*, vol. 44, no. 12, pp. 4864–4883, Dec. 2015.
- [35] N. Lower and R. Wilcoxon, "Alkali silicate glass based thermal coatings," in *Proc. 26th Annu. IEEE Semiconductor Thermal Meas. Manage. Symp. (SEMI-THERM)*, Feb. 2010, pp. 93–99.
- [36] N. P. Lower, A. P. Boone, and R. K. Wilcoxon, "Integrated circuit tampering protection and reverse engineering prevention coatings and methods," U.S. Patent 8084855B2, Dec. 27, 2011.
- [37] N. P. Lower, A. P. Boone, and R. K. Wilcoxon, "Adhesive applications using alkali silicate glass for electronics," U.S. Patent 8637980 B1, Jan. 28, 2014.
- [38] N. P. Lower, R. K. Wilcoxon, A. P. Boone, N. P. Wyckoff, and B. C. Hamilton, "Glass thick film embedded passive material," U.S. Patent 8119040 B2, Feb. 21, 2012.
- [39] N. P. Lower, R. K. Wilcoxon, and A. P. Boone, "Integrated circuit protection and ruggedization coatings and methods," U.S. Patent 8076185 B1, Dec. 13, 2011.
- [40] N. P. Lower, A. P. Boone, R. K. Wilcoxon, and D. D. Hillman, "Alkali silicate glass based coating and method for applying," U.S. Patent 8617913 B2, Dec. 31, 2013.
- [41] R. K. Wilcoxon, N. P. Lower, and A. P. Boone, "Method for providing near-hermetically coated, thermally protected integrated circuit assemblies," U.S. Patent 8166645 B2, May 1, 2012.
- [42] J. D. Sampica, T. J. Barnidge, J. L. Tchou, N. P. Lower, R. K. Wilcoxon, and S. S. Dudley, "Alkali silicate glass for displays," U.S. Patent 8363189 B2, Jan. 29, 2013.
- [43] N. P. Lower, A. P. Boone, R. K. Wilcoxon, and D. D. Hillman, "Alkali silicate glass based coating and method for applying," U.S. Patent 9565758 B2, Feb. 7, 2017.
- [44] G. Lagaly, W. Tufar, A. Minihan, and A. Lovell, *Silicates. Ullmann's Encyclopedia of Industrial Chemistry*. Weinheim, Germany: Wiley, 2000.
- [45] R. Dupree, D. Holland, and D. S. Williams, "The structure of binary alkali silicate glasses," *J. Non-Crystalline Solids*, vol. 81, nos. 1–2, pp. 185–200, Apr. 1986.
- [46] F. K. Crundwell, "On the mechanism of the dissolution of quartz and silica in aqueous solutions," *ACS Omega*, vol. 2, no. 3, pp. 1116–1127, Mar. 2017.
- [47] N. Suzuki, S. Kiba, and Y. Yamauchi, "Bimodal filler system consisting of mesoporous silica particles and silica nanoparticles toward efficient suppression of thermal expansion in silica/epoxy composites," *J. Mater. Chem.*, vol. 21, pp. 14941–14947, 2011.
- [48] K. S. Moon, S. D. Hwang, H. G. Yoon, J. H. Ryu, and S. W. Woo, "High filler loading technique and its effects on the reliability of epoxy molding compound," in *Proc. 2nd Electron. Packag. Technol. Conf.*, Dec. 1998, pp. 318–324.
- [49] *FLX-2320-S Thin Film Stress Measurement: User Manual*, Toho Technology, Chicago, IL, USA, 2010.
- [50] J.-H. Zhao, T. Ryan, P. S. Ho, A. J. McKerrow, and W.-Y. Shih, "Measurement of elastic modulus, Poisson ratio, and coefficient of thermal expansion of on-wafer submicron films," *J. Appl. Phys.*, vol. 85, no. 9, pp. 6421–6424, May 1999.

- [51] K. R. Williams, K. Gupta, and M. Wasilik, "Etch rates for micromachining processing-part II," *J. Microelectromech. Syst.*, vol. 12, no. 6, pp. 761–778, Dec. 2003.
- [52] H. F. Shermer, "Thermal expansion of binary alkali silicate glasses," *J. Res. Nat. Bur. Standards*, vol. 57, no. 2, pp. 97–101, 1956.
- [53] V. Carias *et al.*, "Development of mold compounds with ultralow coefficient of thermal expansion and high glass transition temperature for fan-out wafer-level packaging," *IEEE Trans. Compon., Packag., Manuf. Technol.*, vol. 5, no. 7, pp. 921–929, Jul. 2015.
- [54] K. Lee, M. S. Kim, J. Kim, S. Kim, D. Lee, and K. Jung, "Improvement of package warpage through substrate and EMC optimization," in *Proc. China Semiconductor Technol. Int. Conf. (CSTIC)*, Mar. 2018, pp. 1–4.
- [55] R. Tummala, N. Nedumthakady, S. Ravichandran, B. DeProspero, and V. Sundaram, "Heterogeneous and homogeneous package integration technologies at device and system levels," in *Proc. Pan Pacific Microelectron. Symp. (Pan Pacific)*, Feb. 2018, pp. 1–5.
- [56] H. H. Weldes, "Amine and ammonium silicate solutions," *Ind. Eng. Chem. Product Res. Develop.*, vol. 9, no. 2, pp. 249–253, Jun. 1970.



Vladimir Liberman received the B.A. degree in physics from Princeton University, Princeton, NJ, USA, in 1986, and the Ph.D. degree in applied physics from Columbia University, New York, NY, USA, in 1991.

He has been with the MIT Lincoln Laboratory, Lexington, MA, USA, since December 1996. For the first 20 years, he has pursued the development of novel materials, devices, and nanostructures for wavefront manipulation, energy harvesting, and chemical detection. Most recently, he joined the Active Optical Systems Group, MIT Lincoln Laboratory, where he has leveraged novel technologies and analysis methods for infrared search and track system applications. He has coauthored two book chapters and over 100 articles in conference proceedings and refereed publications.



James C. McRae received the B.S. degree in chemical engineering from the Worcester Polytechnic Institute (WPI), Worcester, MA, USA, in 2019. He is currently pursuing the Ph.D. degree with the Mechanical Engineering Department, Massachusetts Institute of Technology (MIT), Cambridge, MA, USA, in the group of Dr. Carlo Giovanni Traverso supported by the School of Engineering Fellowship.

He has previous materials science and microfabrication research experience in academic, industry, and federal government research settings, most recently

as a Student Technical Assistant at the MIT Lincoln Laboratory, Lexington, MA, USA. He is developing novel ingestible electronic devices at MIT.



Caitlin Rock received the B.S. degree in earth system sciences and geography from Fitchburg State University, Fitchburg, MA, USA, in 2012.

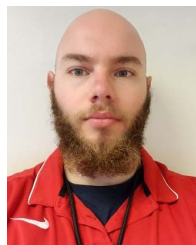
She joined the MIT Lincoln Laboratory, Lexington, MA, USA, in 2016, where she is currently a Senior Technician with the Advanced Imager Technology Group and works on the backside processing of III/V materials, specifically in material thinning and polishing.



Melissa A. Smith (Member, IEEE) received the B.S. degree in materials science and engineering from the University of Illinois at Urbana–Champaign, Urbana, IL, USA, in 2006, and the Ph.D. degree in materials science and engineering from the Massachusetts Institute of Technology (MIT), Cambridge, MA, USA, in 2012.

She is an Assistant Leader of the Advanced Materials and Microsystems Group, MIT Lincoln Laboratory, Lexington, MA, USA, where she is exploring new methods and strategies to build microsystems

and nanoscale devices.



Devon Beck received the B.S. degree in chemistry from Oakland University, Rochester, MI, USA, in 2019.

He has worked on the development of advanced materials chemistries in industry and national lab settings. He is currently a Specialist in additive manufacturing and chemistry with the MIT Lincoln Laboratory, Lexington, MA, USA.



Bradley P. Duncan received the B.A. degree in chemistry from the Saint Anselm College, Manchester, NH, USA, in 2009, and the Ph.D. degree in organic chemistry from the University of Massachusetts at Amherst, Amherst, MA, USA, in 2016.

He is currently a member of the Technical Staff with the Advanced Materials and Microsystems Group, MIT Lincoln Laboratory, Lexington, MA, USA, where he is exploring synthetic modification of nanomaterials and metastable chemical systems.



Livia M. Racz received the B.S. and Ph.D. degrees in materials science and engineering from the Massachusetts Institute of Technology (MIT), Cambridge, MA, USA, in 1989 and 1993, respectively.

She was an Alexander von Humboldt Fellow with the German Aerospace Center (DLR) (formerly German Aerospace Research Center (DLR)), Cologne (Köln), Germany. She joined the MIT Lincoln Laboratory, Lexington, MA, USA, in February 2015, after over eight years at the Draper Laboratory, Cambridge, MA, USA, where she held positions of a Principal Technical Staff, a Distinguished Technical Staff, a Laboratory Technical Staff, the Group Leader, and the Division Leader. She has also spent time in two early stage startups and in academia, focused on novel miniature electronic systems. She is currently an Associate Leader of the Advanced Materials and Microsystems Group, MIT Lincoln Laboratory, where she is focused on advanced materials and their application of microtechnology and nanotechnology, in order to enable unique capability in microsystems. Her program highlights include energetic materials for novel microbatteries, 1-D, 2-D, and 3-D materials integration platforms and techniques, and emerging capability in materials by design. In addition, she leads the MIT Lincoln Laboratory Research Portfolio in advanced materials and processes.



Eric Holihan received the B.S. and M.S. degrees in mechanical engineering from the State University of New York at Buffalo, Amherst, NY, USA, in 2002.

Since 2008, he has been working as a fabrication/research engineer with both startup companies and large defense contractors in the areas of microelectronics and applied nanomaterials research. He is currently an Associate Staff Member with the MIT Lincoln Laboratory, Lexington, MA, USA.